Nanoscale

COMMUNICATION

View Article Online
View Journal | View Issue

Cite this: *Nanoscale*, 2025, **17**, 9122

Received 24th January 2025,
Accepted 10th March 2025

DOI: 10.1039/d5nr00353a

rsc.li/nanoscale

An integrated multimethod approach for size-specific assessment of potentially toxic element adsorption onto micro- and nanoplastics: implications for environmental risk†

Swaroop Chakraborty, *[a] Roland Drexel,[b] Prathmesh Bhadane, [a,c] Nathan Langford,[a] Pankti Dhumal,[a] Florian Meier [b] and Iseult Lynch [a]

Micro- and nanoscale plastics (MnPs), arising from the environmental degradation of plastic waste, pose significant environmental and health risks as carriers for potentially toxic element (PTE) metals. This study employs asymmetrical flow field-flow fractionation (AF4) coupled with multi-angle light scattering (MALS) and inductively coupled plasma mass spectrometry (ICP-MS) to provide a size-resolved assessment of chromium (Cr), arsenic (As), and selenium (Se) adsorption onto carboxylated polystyrene nanoparticles (COOH-PSNPs) of 100 nm, 500 nm, and 1000 nm. Cr exhibited the highest adsorption, with adsorption per particle surface area increasing from 9.45×10^{-15} µg nm^{-2} for 100 nm particles to 6.87×10^{-14} µg nm^{-2} for 1000 nm particles, driven by chemisorptive interactions with carboxyl groups. In contrast, As and Se exhibited slower adsorption rates and significantly weaker interactions, attributed to outer-sphere complexation and electrostatic repulsion. Smaller particles exhibited enhanced adsorption efficiency per unit mass due to their larger surface area-to-volume ratios and higher carboxyl group density (18.5 µEq g^{-1} for 100 nm compared to 7.9 µEq g^{-1} for 1000 nm particles). Se adsorption remained negligible across all sizes, near detection limits, highlighting its low affinity for carboxylated surfaces. Our study demonstrates the superior resolution of AF4-MALS-ICP-MS compared to that of bulk ICP-MS, which lacks the ability to discern particle-specific adsorption trends. Unlike bulk ICP-MS, which provides average adsorption values, AF4-MALS-ICP-MS reveals the size-dependent mechanisms influencing metal binding, offering critical insights into the role of MnPs as PTE vectors. The findings highlight the environmental implications of MnPs in facilitating PTE transport and highlights the need for size-specific mitigation strategies. This work sets a foundation for developing more precise risk assessment frameworks and advanced remediation approaches for MnP-contaminated environments.

1. Introduction

Micro- and nanoplastics (MnPs) are increasingly recognised as pollutants of global concern, particularly within aquatic ecosystems.[1] These particles, typically less than 5 mm in size, result from the degradation of larger plastics or are intentionally manufactured for various commercial applications[2] although intentional uses are being phased out due to the problems associated with MnPs.[3] Their small size and large surface area allow MnPs to act as vectors for environmental contaminants, including PTEs and persistent organic pollutants, posing a significant threat to aquatic life and human health.[4] Studies have shown that MnPs have an affinity for PTEs, which adhere to their surfaces, leading to the bioaccumulation of these toxins across the food web.[5,6] Despite this growing recognition, the mechanisms driving the adsorption of PTEs onto MnPs remain poorly understood, particularly with respect to the influence of the physicochemical properties of the MnPs, such as size, surface charge, and chemical composition.[7,8]

In this context, the coupling of asymmetrical flow field-flow fractionation (AF4) with multi-angle light scattering (MALS) and inductively coupled plasma mass spectrometry (ICP-MS) represents a significant advancement in the study of MnPs and their interactions with PTEs.[9–11] AF4, as an advanced separation technique, enables the fractionation of MnPs based on their hydrodynamic size without altering their native state, which is crucial for understanding how different sized particles behave in environmental systems.[12] When combined with MALS, the technique provides precise real-time measurements of particle size and shape, while ICP-MS offers highly sensitive quantification of metal adsorption on MnPs, even at trace levels (<ng L^{-1}). This hyphenated technique is particularly innovative because it overcomes the limitations of tra-

---

[a] *School of Geography, Earth & Environmental Sciences, University of Birmingham, Edgbaston, B15 2TT, UK. E-mail: s.chakraborty@bham.ac.uk*
[b] *Postnova Analytics GmbH, Landsberg am Lech, Germany*
[c] *Indian Institute of Technology, Gandhinagar, 382055, India*

† Electronic supplementary information (ESI) available. See DOI: **https://doi.org/10.1039/d5nr00353a**

ditional bulk adsorption studies, which often fail to differentiate between various size fractions of MnPs or provide accurate quantification of adsorbed metals. The AF4-MALS-ICP-MS system allows simultaneous characterisation of particle size and metal content, providing a comprehensive understanding of how these factors influence PTE fouling on MnP surfaces.[13] Asymmetric flow field-flow fractionation coupled with inductively coupled plasma mass spectrometry (AF4-ICP-MS) has been extensively applied to characterise the interactions of trace elements in natural and engineered colloidal systems. Previous studies have demonstrated its utility in examining the binding and transport of rare earth elements within iron–organic matter nanocolloids in an Alaskan river.[14] Additionally, AF4-ICP-MS has been employed to study mercury complexation within the natural colloidal pool, providing insights into mercury mobility and transformation processes in polluted environments.[15] The technique has also been used to quantify the adsorption of heavy metals such as copper and lead onto quantum dots, as well as uranium onto iron-oxide ferrihydrite.[16] These studies highlight the versatility of AF4-ICP-MS in probing metal–colloid interactions and provide a framework for its application in emerging areas of research, such as the adsorption of trace elements onto nanoplastics. Such insights are critical for advancing our understanding of the environmental fate of MnPs in real environmental samples and their potential risks. Recent studies have highlighted the role of nano-colloids in controlling the adsorption and mobility of PTEs. Tadayon *et al.* (2024) investigated rare earth element (REE) interactions with synthetic mixed colloids using AF4-ICPMS, demonstrating that REE adsorption induces colloidal aggregation, significantly influencing environmental mobility.[17] To strengthen our approach, Faucher *et al.* (2018) combined MALS and ICP-MS to characterise quantum dots in a natural matrix, showcasing how advanced fractionation techniques enhance the understanding of nanoparticle behavior in complex environmental media.[18] Additionally, Worms *et al.* (2012) assessed the impact of nanoparticle interactions on metal bioavailability in microalgae, providing critical insights into how engineered nanomaterials modulate trace metal uptake and toxicity.[19] These studies collectively validate our methodology and reinforce the environmental implications of our findings.

The importance of this work is highlighted by the fact that MnPs are now ubiquitous in global water systems, with significant implications for ecosystems and food safety. PTE contamination, exacerbated by the presence of MnPs, contributes to the long-term persistence of toxic substances in the environment.[5,20,21] By employing AF4-MALS-ICP-MS, this study addresses key knowledge gaps in assessing and quantifying MnP interactions (particularly particles <1000 nm) with PTE co-pollutants, offering a novel and robust approach for studying the environmental behaviours of MnPs with PTE fouling. The outcomes of this research could have far-reaching implications, informing the development of mitigation strategies for plastic pollution and setting a new benchmark for environmental risk assessments of emerging contaminants.

2. Experimental section

2.1. Materials

Carboxylated polystyrene micro- and nanoplastics (COOH-PSNPs) of three different sizes—100 nm, 500 nm, and 1000 nm at a concentration of 4 wt% solid—were procured from Thermo Fisher Scientific, UK. All chemicals used in the experiments were of analytical grade.

ICP standards of chromium (Cr), arsenic (As), and selenium (Se) in 2% nitric acid were procured from PerkinElmer, USA, with the following oxidation states: Cr(III) (chromium(III) standard solution, present as $Cr(H_2O)_6{}^{3+}$), As(V) (arsenic(V) standard solution, present as $H_2AsO_4{}^{-}$), Se(IV) (selenium(IV) standard solution, present as H_2SeO_3). These oxidation states were selected based on their environmental relevance and their influence on adsorption behaviour onto MnPs. The metal/metalloid solutions were prepared at a final concentration of 1 μg mL^{-1} (1 mg L^{-1}) in 1 mM HEPES buffer (pH 7.4) with 1 mM EDTA—to investigate adsorption dynamics.

2.2. Characterisation of carboxylated polystyrene nanoplastics

The COOH-PSNPs MnPs were characterised to evaluate their morphology, size distribution, surface chemistry, and stability under varying conditions. These analyses were conducted on both pristine samples and post-adsorption of PTEs (Cr, As, and Se) to determine any physicochemical changes resulting from metal binding. Scanning electron microscopy (SEM, Aprio Thermo) was employed to examine the surface morphology of the COOH-PSNPs. High-resolution imaging confirmed the spherical shape and uniform size distribution, and SEM also provided information on surface modifications and potential agglomeration after metal ion exposure. Dynamic light scattering (DLS, Malvern Zeta Sizer, UK) measurements, conducted at a MnP concentration of 0.05% (w/v), provided hydrodynamic size data across pH values (2, 4, 6, 8, 10, and 12). These measurements assessed the colloidal stability of the COOH-PSNPs before and after PTE adsorption, indicating changes in particle size and agglomeration behaviour in response to pH and metal ion binding. Transmission electron microscopy (TEM, Jeol 1400) provided higher-resolution images of the COOH-PSNPs, confirming their core size and revealing structural changes post-adsorption, including potential agglomeration or morphological modifications. Fourier-transform infrared spectroscopy (FTIR, PerkinElmer, USA) was used to characterise surface functional groups, verifying the presence of carboxyl groups. The measurement was performed on all COOH-PSNPs both pre- and post-adsorption of PTE metals. Zeta potential measurements were performed to evaluate surface charge changes across a pH range (2–12), both pre- and post-metal adsorption.

2.3. PTE adsorption studies

In this study, the adsorption of Cr, As, and Se onto COOH-PSNPs of three sizes (100 nm, 500 nm, and 1000 nm) was investigated. The metal ion solutions were prepared from

1000 μg mL^{-1} (1 mg mL^{-1}) ionic standards, resulting in a final metal ion concentration of 1 μg mL^{-1} (1 mg L^{-1}) in two different media: deionised water (DI) and 1 mM HEPES with 1 mM EDTA (pH 7.4). While 1 mg L^{-1} is not particularly low for environmental analyses, this concentration was selected to evaluate whether AF4-MALS-ICP-MS could sensitively and accurately quantify metal adsorption onto nanoplastics after the adsorption process. It is important to note that using a single concentration does not establish the method's limit of detection (LOD), which typically requires multiple concentration levels or replicate measurements at different spikes. Additionally, the 1 μg mL^{-1} (1 mg L^{-1}) metal ion concentration was chosen to ensure detectability and reliable quantification of adsorption using AF4-ICP-MS. While environmental concentrations of Cr, As, and Se vary, this controlled concentration allows for standardised adsorption studies, ensuring reproducibility and comparability across different conditions.

A 0.05% (from a 4 wt% stock) suspension of COOH-PSNPs was added to 50 mL of the metal ion solutions and incubated for seven days under gentle agitation, following established adsorption protocols. In addition to individual size fractions, a mixed sample was prepared by combining 100 nm, 500 nm, and 1000 nm COOH-PSNPs at 1.33 wt% and subsequently diluting it to a final working concentration of 0.05% for AF4-MALS-ICP-MS analysis. To verify accuracy, the AF4 recovery of both the nanoplastics and the metal ions was monitored by comparing the injected mass to that recovered in the collected fractions. Future work involving multiple concentrations would be required to fully determine the system's LOD and further validate the method's performance. The value of 1 μg mL^{-1} metal ion concentration was considered by taking into account high-exposure and contamination areas. A mixture of these PTEs (at a concentration of 1 μg mL^{-1}) was prepared before adding the COOH-PSNPs to the solution. Also, individual PTE adsorption at a concentration of 1 μg mL^{-1} was also performed at a similar concentration of COOH-PSNPs. Cr concentrations can reach 10–50 μg L^{-1} in water, 100–500 mg kg^{-1} in soil, and 10–200 ng m^{-3} in air, often near tanneries or electroplating industries.[22,23] Hotspots for As, like Bangladesh, show groundwater levels of 100–3000 μg L^{-1}, soil up to 1000 mg kg^{-1}, and air near smelters at 10–100 ng m^{-3}.[22–26] Se in irrigation basins (*e.g.*, California) can exceed 500 μg L^{-1} in water, 100 mg kg^{-1} in soil, and 50–500 ng m^{-3} in air near coal plants.[27,28] After incubation, samples were filtered using 0.02-micron syringe filters to remove the COOH-PSNPs, while the unbound metal ions passed through in solution. Metal concentrations in the filtrate were measured using inductively coupled plasma mass spectrometry (ICP-MS, Nexion 350, PerkinElmer, USA), operated in helium kinetic energy discrimination (KED) mode at 4 mL min^{-1} Helium purging was used to minimise polyatomic interferences during metal quantification (PerkinElmer, 2019). The adsorption efficiency, kinetics and selectivity were determined by comparing the initial and final concentrations of metals in the filtrate, with the amounts adsorbed onto the COOH-PSNPs calculated using the difference between the initial concentration of PTEs and the final concentration after adsorption. All experiments were performed in triplicate to ensure reproducibility and reliability. Blank controls without COOH-PSNPs were included to account for any non-specific adsorption of the metal ions onto the filtration system and glassware.

2.4. Estimation of PTE adsorption by hyphenated AF4-MALS-ICP-MS

All PTE adsorbed COOH-PSNP particles were fractionated and characterised using multi-detector AF4 (AF2000-MT system, Postnova Analytics, Landsberg am Lech, Germany (PN)). In the analytical channel with a tip-to-tip length of 277 mm a 10 kDa regenerated cellulose membrane was installed. The nominal channel height was defined by a 350 μm spacer. The channel was thermally controlled at 25 °C. The AF4 system was equipped with an autosampler (PN5300), a UV/Vis detector (PN3211) and a 21-angle MALS detector (PN3621). The MALS detector operated at a wavelength of 532 nm. All angles were normalized with respect to the 90° angle at the peak maximum of a fractionated 60 nm polystyrene bead certified size standard using a spherical scattering model (60 nm ± 4 nm at a concentration of 1% (w/w) Nanosphere™ Size Standard 3060A, Thermo Fisher Scientific, Waltham, MA, USA). An ICP-MS (7900 ICP-MS, Agilent Technologies Inc., USA) was hyphenated directly to the MALS detector. The ICP-MS system consisted of a MicroMist nebulizer and a Scott spray chamber. The plasma gas flow rate was 17 L min^{-1}, whereas the nebuliser gas flow rate was 1.05 mL min^{-1}. All measurements were conducted at a maximum radio frequency (RF) power of 1550 W. Potential polyatomic interferences were removed by introducing a 4.5 mL min^{-1} helium flow into the collision cell. The ICP-MS performance was checked daily with a performance test. The isotopes of ^{52}Cr, ^{75}As and ^{78}Se were monitored with integration times of 0.3 s, 0.3 s and 1.0 s, respectively. A multi-element ICP-MS standard (CPAChem Ltd, Bogomilovo, Bulgaria) was used for calibration. The calibration standards (1 ng mL^{-1}, 5 ng mL^{-1}, 10 ng mL^{-1}, 20 ng mL^{-1} and 50 ng mL^{-1}) were diluted in the AF4 carrier liquid (0.025% NovaChem) and were introduced *via* a T-piece using a peristaltic pump with the AF4 system delivering a constant flow rate to another port of the T-piece to have a total flow rate of 0.50 mL min^{-1} going to the nebuliser. The carrier liquid in AF4 is a crucial component, as it facilitates the separation and elution of particles based on size, density, or other physicochemical properties.

A carrier liquid consisting of 0.025% NovaChem (PN) was used throughout all fractionations. The AF4 fractionation method was operated at a constant detector flow rate of 0.5 mL min^{-1}. The flow rates were stabilised for 2 min, and then the injection was carried out. After 5 min of focusing at an initial cross-flow rate of 1 mL min^{-1} and an injection flow rate of 0.2 mL min^{-1}, a transition time of 0.5 min was used to change to elution mode. The initial cross-flow rate was maintained constant for 0.2 min, followed by a 40 min long power decay to a cross-flow rate of 0.05 mL min^{-1}, which was maintained constant for 25 min. A rinse step of 12 min at 0.6 mL min^{-1} was applied to reduce potential carryover and memory effects. Fig. S1† illustrates the AF4 flow programming, outlining the three distinct phases of focusing, elution, and rinsing, which were applied consistently across all samples to achieve effective fractionation. Fig. S4† presents the reference fractograms obtained from AF4-MALS analysis of native COOH-PSNPs (100 nm, 500 nm, and 1000 nm), showing distinct elution profiles corresponding to each particle size based on the MALS 90° signal.

The MALS data analysis was carried out using the NovaAnalysis Software (PN, Version 2408). The software was also used to merge all detector traces including ICP-MS traces. MALS data were analysed using the sphere model and 19 active angles over an angular range of 12° to 156°. Signal processing and additional calculations were performed using Excel (Version 2410, Microsoft 365) and Origin 2019 (Version 9.6.0.172, Origin Lab Corporation). Particle number calculations from MALS scattering data were conducted based on the work of Kerker (1969).[29] All quantitative results are normalised to 1 μL of suspension that was injected into the AF4-MALS-ICP-MS system. Incubated samples were tip-sonicated for 1 min in pulse mode to prevent thermal influence (5 mm tip, 0.5 s on, 0.5 s off, 40% amplitude, Hielscher Ultrasonics GmbH, Teltow, Germany). After diluting 100 μL of the stock solution of metal ion-incubated COOH-PSNPs in 2.9 mL of AF4 carrier liquid, the suspension was sonicated in an ultrasonication bath at 160 W (Sonorex Digital P10, Bandelin Electronics GmbH, Berlin, Germany) for 5 more minutes. Injection volumes of 50 μL to 100 μL were applied.

3. Results and discussion

3.1. Physicochemical characterisation of COOH-PSNPs

The physicochemical characterisation of the COOH-PSNPs was carried out using multiple analytical techniques to monitor any changes in size, surface charge, and chemical functionality from their pristine state to post-incubation with Cr, As, and Se. Transmission electron microscopy (TEM) images (Fig. 1(A–D)) and SEM images (Fig. 1(E–H) alongside Table 1) provide clear visual evidence of the spherical morphology of the COOH-PSNPs at different magnifications. The TEM images revealed well-separated COOH-PSNPs with uniform size distributions. In particular, Fig. 1 panels (A) and (E) represent the 100 nm COOH-PSNPs which showed a more compact arrangement of smaller COOH-PSNPs, compared to Fig. 1 panels (B) and (F) representing the 500 nm COOH-PSNPs and panels (C) and (G) showing the 1000 nm COOH-PSNPs which demonstrated slightly larger particles and showed a homogeneous distribution of the COOH-PSNPs. Fig. 1D and F present TEM and SEM images of mixed (100 nm, 500 nm and 1000 nm) COOH-PSNPs with some agglomeration. The consistent particle sizes observed in TEM and SEM further correlate with the DLS measurements shown in Fig. 2(B) and Table 1, which indicated that the average hydrodynamic diameter increased with particle size, from around 130 ± 11 nm for the 100 nm COOH-PSNPs to 1150 ± 17 nm for the 1000 nm COOH-PSNPs. This size increment is expected in DLS as compared to TEM as the hydrodynamic diameter (as measured by DLS) in solution is typically larger due to solvation and particle agglomeration, especially for larger particles.[30,31]

The zeta potential data shown in Fig. 2(A) and (C) provide insights into the surface charge and colloidal stability of COOH-PSNPs. Fig. 2(C) shows the zeta potential values measured in deionised water and HEPES buffer for all particle sizes before and after metal adsorption. Pristine COOH-PSNPs exhibit highly negative zeta potentials (∼−70 mV) in both media, indicative of excellent colloidal stability due to electrostatic repulsion. This high negative charge is primarily attribu-

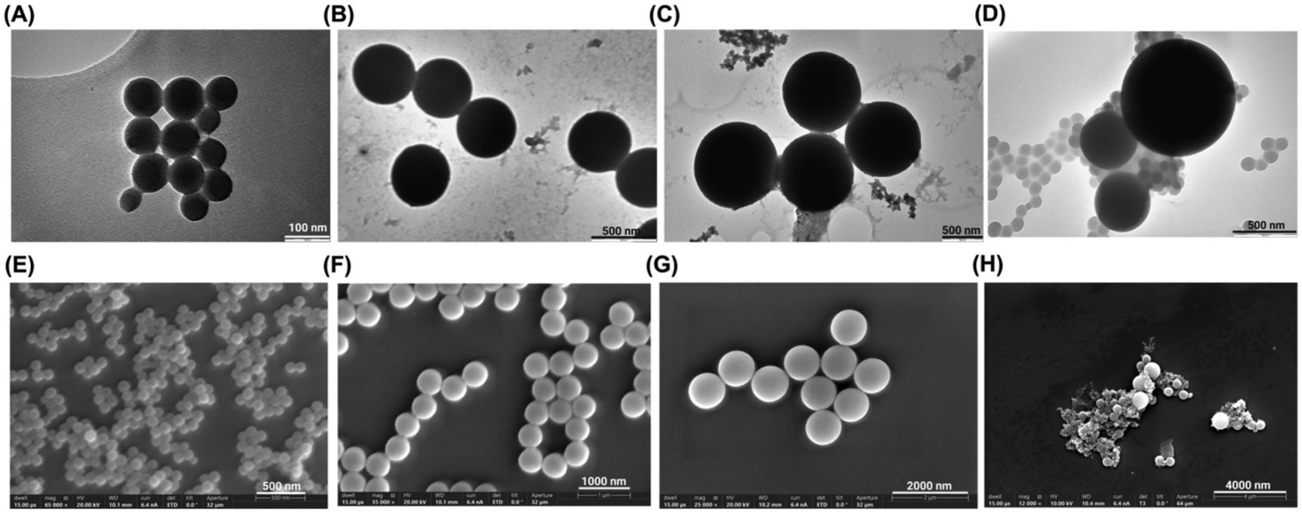

Fig. 1 Characterisation of COOH-PSNPs. Panels (A–D) show TEM images of 100 nm, 500 nm, and 1000 nm COOH-PSNPs, and mixed sizes of COOH-PSNPs, respectively, indicating a uniform spherical morphology. Panels (E–H) display SEM images of COOH-PSNPs of varying sizes post-metal adsorption (1 μg L^{-1} of Cr, Se, and As), with some agglomeration seen in the larger particles. There were no changes in the particle morphology observed by electron microscopy post-adsorption of metal ions.

Table 1 Physicochemical characterisation of COOH-PSNPs

COOH-PSNP particles	TEM (nm)	DLS size (nm)	MALS size R_g (nm)	Zeta potential (mV)	Specific surface area (cm^2 g^{-1})	Number of COOH group per particle	COOH titration (μEq g^{-1})
100 nm	110 ± 10	130 ± 11	44.5 ± 2.29	−55 ± 3	5.2×10^5	8.2×10^3	18.5
500 nm	490 ± 18	550 ± 20	211.0 ± 3.74	−70 ± 5	1.2×10^5	3.8×10^5	9.6
1000 nm	1100 ± 44	1150 ± 17	429.0 ± 5	−70 ± 3.5	5.2×10^4	3.5×10^6	7.9

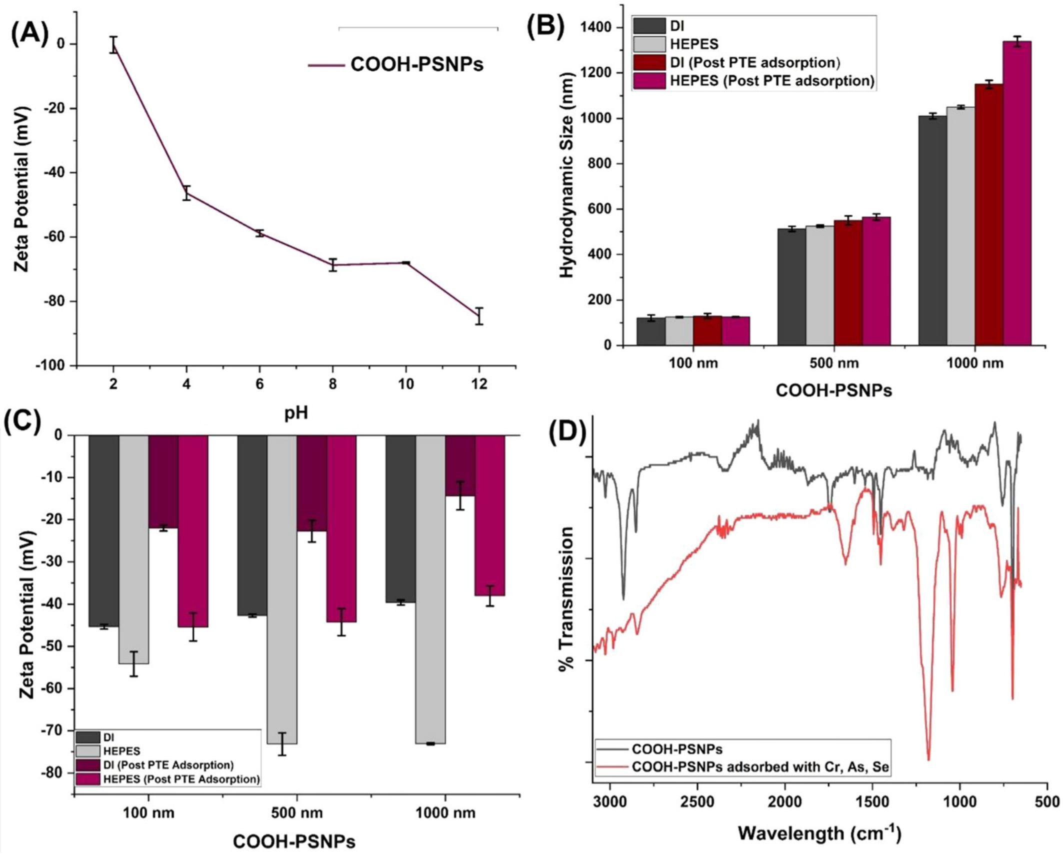

Fig. 2 Characterisation of COOH-PSNPs pre- and post-metal ion adsorption. Panel (A) shows zeta potential variation with pH, reflecting reduced stability at higher pH levels. Panel (B) displays the hydrodynamic size and zeta potential (ZP), which increase after metal ion adsorption, particularly in HEPES + EDTA buffer, indicating particle agglomeration or surface mass increase through ion adsorption. Panel (C) shows zeta potential measurements in deionised water (DI) and HEPES buffer before and after Cr, As, and Se adsorption. The zeta potential becomes less negative post-adsorption, suggesting surface charge neutralization by cationic metal ions, which is consistent with lower electrostatic stabilisation of the particles. Panel (D) provides FTIR spectra of pristine and metal-adsorbed COOH-PSNPs, with shifts in the C=O and O–H regions, suggesting carboxyl group involvement in metal binding.

ted to the ionised carboxyl groups (–COOH) on the surface of the PSNPs, which deprotonate in aqueous environments, generating a strong negative surface charge.[32] After metal adsorption, the zeta potential becomes less negative, especially in HEPES buffer. This shift indicates that the positively charged metal ions (Cr, As, and Se) are neutralising some of the negative charges on the PSNP surface, forming surface complexes. Such a reduction in zeta potential is typical of PTE binding, where the adsorption of cations neutralises the surface charges, potentially decreasing the colloidal stability of the particles.[33] Fig. 2(A) further corroborates this observation by showing the pH-dependent zeta potential of COOH-PSNPs, whereby the zeta potential becomes more negative with increasing pH, highlighting that the COOH-PSNPs are unstable under acidic to neutral conditions but exhibit higher stability in more alkaline environments.[34] The hydrodynamic size measurements, shown in Fig. 2(B), indicate an increase in particle size post-metal adsorption, especially for the larger 500 nm and 1000 nm COOH-PSNPs. This increase in size is consistent with the formation of metal-ion complexes on the surface of the COOH-PSNPs, where the binding of metal ions such as Cr, As, and Se could lead to agglomeration or an increase in particle size due to the increased surface mass. The hydrodynamic size increased more in HEPES buffer than in deionised water, further supporting the enhanced metal complexation in buffer systems, which may stabilise the metal ions in solution and promote surface adsorption.

The number of carboxylic groups per particle (Table 1), specific surface area, and COOH titration for COOH-functionalised polystyrene nanoparticles (COOH-PSNPs) vary significantly across particle sizes. For 100 nm particles, the specific surface area is 5.2×10^5 cm^2 g^{-1}, with 8.2×10^3 COOH groups per particle and a COOH titration of 18.5 μEq g^{-1}, while the zeta potential is −55 mV in deionised water, indicating decent electrostatic stability. In contrast, 500 nm particles have a reduced surface area of 1.2×10^5 cm^2 g^{-1}, 3.8×10^5 COOH groups per particle, and a lower COOH titration of 9.6 μEq g^{-1}, with a more negative zeta potential of −70 mV, suggesting higher electrostatic repulsion. For the 1000 nm particles, the surface area decreases further to 5.2×10^4 cm^2 g^{-1}, but the number of COOH groups increases to 3.5×10^6 per particle, with the lowest COOH titration at 7.9 μEq g^{-1} and a zeta potential of −70 mV. The increasing zeta potential with size indicates stronger surface charge stabilisation despite the reduced specific surface area. These data were crucial in calculating the adsorption of Cr, As and Se on various sizes of COOH-PSNPs and their dependence on surface area and functional group density as determined using AF4-MALS-ICP-MS.

The FTIR spectra (Fig. 2D) of COOH-PSNPs before and after adsorption of Cr, As, and Se revealed critical insights into the interaction between these PTEs and the MnPs' surface functional groups. The pristine MnPs (black spectrum) exhibited distinct peaks corresponding to the carboxyl groups (–COOH) and hydroxyl groups (–OH), particularly the C=O stretching near ∼1700 cm^{-1} and O–H stretching between ∼3000–3500 cm^{-1}.[35] After metal adsorption (red spectrum), there was a significant reduction in transmission in these regions, indicating metal binding through surface complexation. This binding suggests that the metals form coordination complexes with the oxygen atoms of the carboxyl groups, a phenomenon widely reported in the literature for PTE adsorption onto oxygenated functional groups.[36,37] Moreover, the appearance of new bands in the lower wavenumber region (∼500–800 cm^{-1}) strongly indicated the formation of metal–oxygen bonds (Cr–O, As–O, Se–O), confirming direct metal–ligand interactions.[38,39]

Further analysis showed that post-adsorption, there were notable shifts in the C–O stretching region (∼1200–1300 cm^{-1}), again supporting the formation of complexes between metal ions and the oxygen-containing groups on the MnPs. The decrease in intensity of the O–H and C=O peaks reflects the involvement of hydroxyl and carboxyl groups in the binding process. These observations are consistent with the known mechanism of PTE adsorption, where Cr, As, and Se form coordination complexes with the carboxyl groups on MnPs, altering the surface chemistry.[40] This strong interaction between metals and the surface of the COOH-PSNPs can lead to enhanced stability and persistence of these contaminants in the environment. Such behaviour is of significant concern in aquatic systems, where MnPs can act as vectors for the transport of toxic metals, potentially increasing their mobility and bioavailability, which poses long-term ecological risks.[41,42]

3.2. Adsorption studies

The adsorption characteristics of PTEs, including Cr, As, and Se, onto COOH-PSNPs were investigated to understand the influence of surface chemistry and MnP size on metal binding. COOH-PSNPs of varying sizes (100 nm, 500 nm, 1000 nm, and mixed sizes) were used to study adsorption behaviour. Fig. 3 and 4 illustrate the adsorption behaviour over time and the kinetic modelling using pseudo-first-order (PFO) (Fig. S5†) and pseudo-second-order (PSO) (Fig. 4) models, with kinetic parameters summarised in Table 2. These findings provide insights into the interaction mechanisms and effectiveness of COOH-PSNPs for selective PTE removal in contaminated water systems.

Fig. 3 (panels A–D) shows the time-dependent adsorption of Cr, As, and Se onto COOH-PSNPs, revealing that Cr adsorption rapidly reached equilibrium within the first hour across all particle sizes, with nearly 1.0 μg L^{-1} adsorbed from the solution. This rapid uptake for Cr suggests a high affinity between Cr ions and the carboxyl groups (–COOH) on the PSNP surface, indicative of chemisorption *via* inner-sphere complexation. This behaviour aligns with studies on metal binding to carboxyl-functionalised MnPs, where Cr ions exhibit strong adsorption due to covalent bonding potential with oxygen atoms on the COOH-PSNP surface.[43,44] As and Se exhibited slower adsorption rates and reached equilibrium at lower adsorption capacities, approximately 0.4 μg L^{-1} and 0.2 μg L^{-1}, respectively. The lower adsorption for As and Se suggests weaker interactions, likely due to outer-sphere complexation or physisorption mechanisms. This slower equilibrium is consistent with the literature indicating that As and Se ions, particularly in their higher oxidation states, form weaker bonds with carboxylated surfaces and may experience electrostatic repulsion due to similar surface charges.[45–48]

To further elucidate the adsorption mechanism, kinetic data were fitted to both PFO (Fig. S4†) and PSO models[49] (Fig. 4), with parameters for both models shown in Table 2. The pseudo-PSO kinetic model was applied using adsorption data obtained from triplicate experiments (n = 3) as presented in Fig. 3. Standard deviations were considered in the adsorption studies, with Cr adsorption showing minimal variation, indicating high reproducibility. While error bars are not explicitly shown in Fig. 4 due to the nature of the kinetic fitting, the consistency of adsorption trends supports the reliability of the model. Across all particle sizes and metals, the PSO model (calculated using eqn (S6)†) exhibited a superior fit ($R^2 > 0.99$), suggesting that chemisorption, which involves the sharing or exchange of electrons between metal ions and COOH-PSNP functional groups, predominantly controls the adsorption process. In contrast, the PFO model (calculated using eqn (S5)†), often associated with physisorption, showed lower R^2 values, indicating that physical adsorption is minimal for metal ion binding on COOH-PSNPs. The high q_e value of

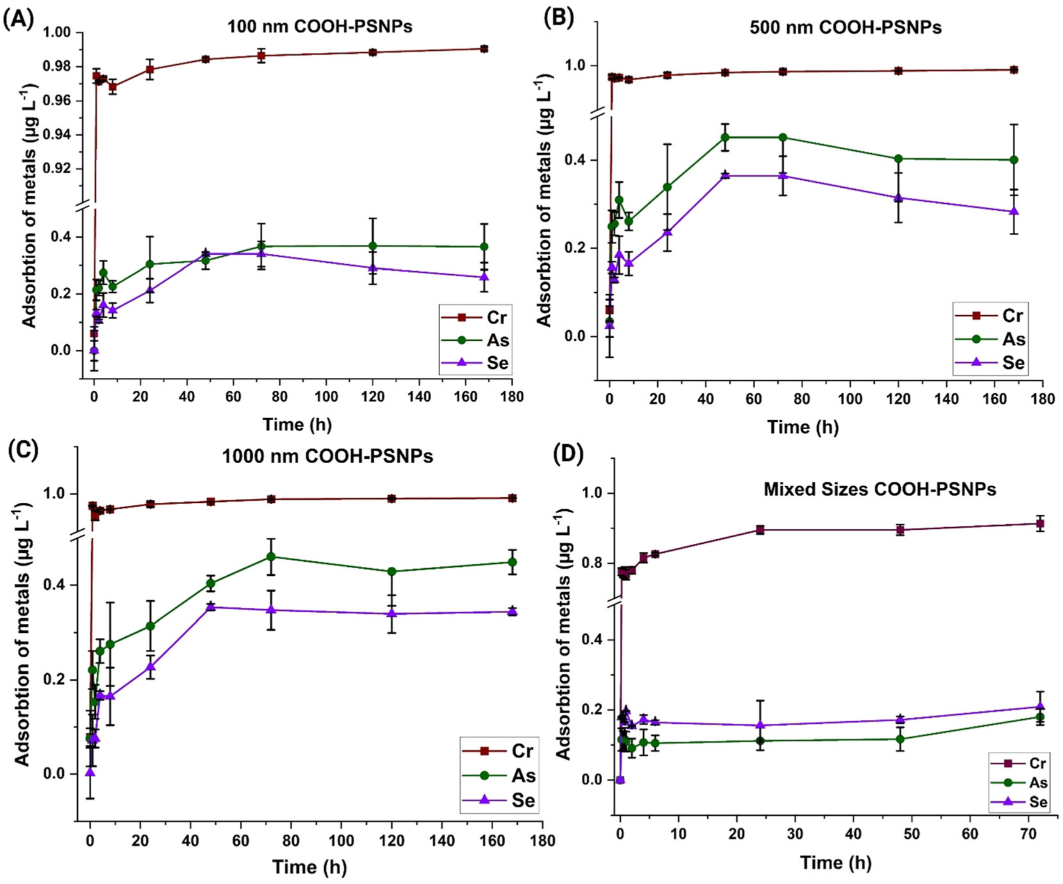

Fig. 3 Time-dependent adsorption analysis of Cr, As, and Se onto COOH-PSNPs. Panels (A–D) depict the adsorption of Cr, As, and Se over time on 100 nm, 500 nm, 1000 nm, and mixed-size PSNP systems, respectively. Adsorption equilibrium for Cr is achieved rapidly (~5 hours), reaching a maximum adsorption of nearly 1.0 μg L^{-1} for all particle sizes, while As and Se adsorption proceed more gradually, stabilising at lower adsorption capacities.

5.769 mg g^{-1} for mixed-size COOH-PSNPs and 0.6289 mg g^{-1} for 100 nm COOH-PSNPs highlights the strong affinity between Cr ions and carboxyl groups. The PSO rate constant (K_2) for Cr adsorption (*e.g.*, K_2 = 0.00949 g mg^{-1} min^{-1} for mixed sizes) further supports the rapid chemisorption mechanism, as Cr ions quickly form stable, inner-sphere complexes with surface –COOH groups. This is corroborated by the FTIR results (Fig. 2D) showing shifts in the C=O stretching (~1700 cm^{-1}) after Cr adsorption, which indicates coordination bonding between Cr and carboxyl groups. For As and Se, the PSO model also fits with lower q_e and K_2 values, indicating weaker interactions. As shows a q_e of 0.993 mg g^{-1} and K_2 of 0.00697 g mg^{-1} min^{-1}, while Se has a q_e of 1.244 mg g^{-1} and K_2 of 0.01187 g mg^{-1} min^{-1}. The slower adsorption rates for As and Se suggest the occurrence of outer-sphere interactions and possibly some physisorption, resulting in less stable and more reversible binding.

The selective adsorption of Cr over As and Se is highlighted by the distribution coefficients (K_d) (calculated using eqn (S1), (S2) and (S3)†) and separation factors (S.F.; calculated using eqn (S4)†).[50] The high K_d values for Cr, especially for 100 nm COOH-PSNPs (779 896.21 mL g^{-1}), relative to As (4556.69 mL g^{-1}) and Se (2679.63 mL g^{-1}), reflect Cr's preferential binding to COOH-PSNPs. The calculated separation factors (*e.g.*, S.F. (Cr/As) = 171.15 and S.F. (Cr/Se) = 291.04 for 100 nm PSNPs) indicate that COOH-PSNPs are significantly more selective for Cr ions than for either As or Se, consistent with other studies where Cr demonstrates stronger chemisorptive interactions with carboxylated surfaces.[51]

The adsorption capacity of COOH-PSNPs for Cr, As, and Se decreases with increasing particle size. Smaller particles (100 nm) consistently exhibit higher adsorption capacities, likely due to their larger surface area-to-volume ratios, which provide more accessible active sites for binding. For instance, the adsorption capacity at equilibrium, q_e, of Cr on 100 nm PSNPs is higher than that on 1000 nm PSNPs, suggesting that smaller MnPs enhance adsorption efficiency through increased surface availability, whereas the larger particles (1000 nm) show higher adsorption per COOH group due to the presence of higher number of COOH group on their surface. Interestingly, the effect of particle size is more pronounced for Cr than for As, due to Cr's stronger chemisorptive interactions, whereby additional surface area and more COOH groups lead to more covalent bonding sites for Cr ions. For As and Se,

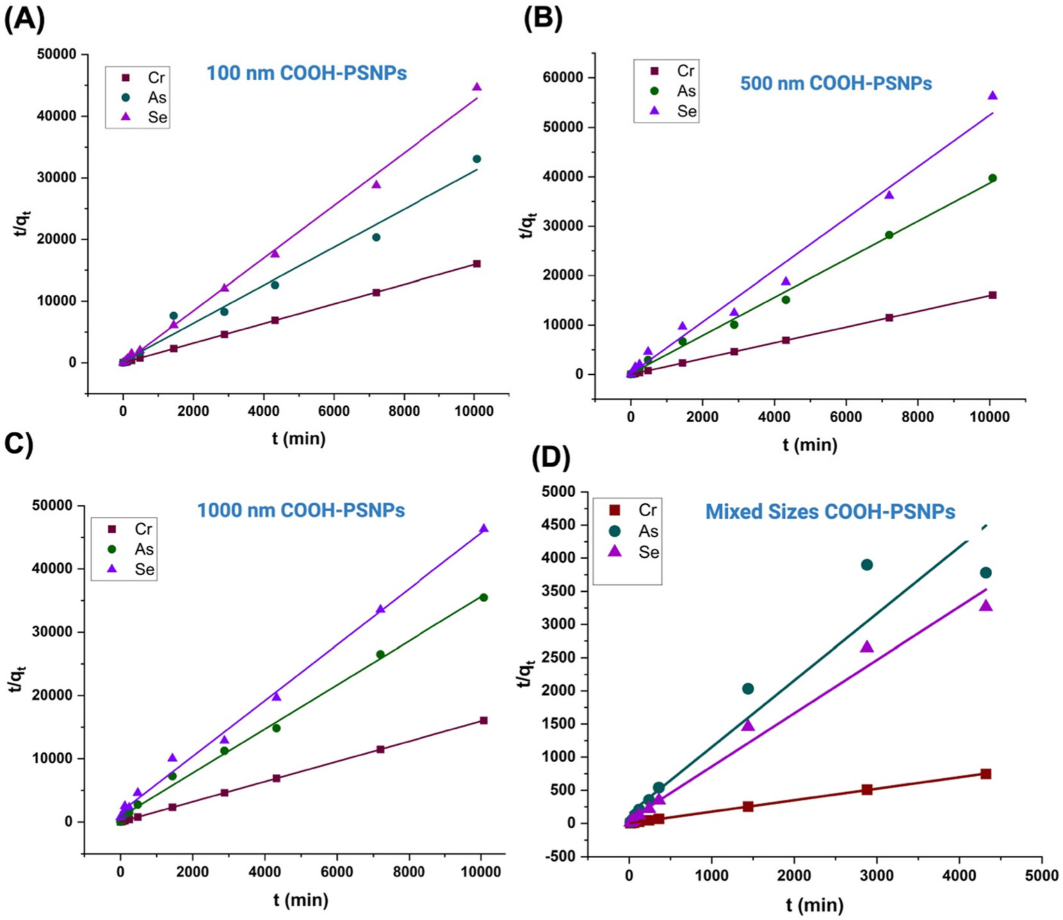

Fig. 4 Adsorption kinetic analysis of Cr, As, and Se onto COOH-PSNPs. The figure shows the pseudo-second order (PSO) kinetic fitting for the adsorption of Cr, As, and Se on the 100 nm (A), 500 nm (B), 1000 nm (C), and mixed-size systems (D), respectively. The excellent fit of the PSO model (R^2 > 0.99) confirms that chemisorption is the dominant mechanism for all metals, with Cr exhibiting the highest adsorption capacity and Se the lowest. The data demonstrate that smaller COOH-PSNPs have slightly higher adsorption capacities due to increased surface area-to-volume ratios, which provide more active sites for metal binding. The adsorption kinetics and capacity are closely linked to the surface chemistry of the PSNPs, as well as to the specific interactions between each metal ion and the carboxyl groups (–COOH) on the COOH-PSNP surfaces.

which primarily interact *via* weaker forces, the increase in surface area with smaller particles does not substantially impact adsorption capacity.

The FTIR spectra (Fig. 2, panel D) revealed significant changes in the C═O stretching region (~1700 cm^{-1}) after Cr adsorption, supporting the formation of inner-sphere complexes between Cr ions and carboxyl groups on COOH-PSNPs. In contrast, As and Se binding induced smaller shifts, indicating weaker binding likely due to physisorption or outer-sphere complexation. This selective interaction with Cr corroborates the PSO kinetic model, confirming that Cr binds through chemisorption, while As and Se primarily interact through physical or weaker chemical forces. The FTIR findings support existing literature where Cr is shown to form stronger covalent bonds with oxygen-containing groups,[52,53] and from its binding stability on carboxylated MnPs. This mechanism is further validated by the high q_e and K_d values for Cr (Table 2), demonstrating the practical potential of COOH-PSNPs for selective Cr removal from environmental media.

3.3. Quantification of Cr, As and Se adsorption by AF4-MALS-ICP-MS

The adsorption behaviour of Cr, As, and Se onto COOH-PSNPs was systematically evaluated using AF4-MALS-ICP-MS. This advanced technique provides insights into size-dependent adsorption efficiencies and allows for a detailed comparison of PTE uptake across individual particle sizes and their mixtures. The fractograms in Fig. S2† indicate that while distinct elution profiles are observed for the 100 nm, 500 nm, and 1000 nm COOH-PSNPs in DI water, significant agglomeration occurs, particularly for the 100 nm COOH-PSNPs, as evidenced by the bimodal peak pattern in the MALS 90° signal. The radius of gyration (R_g) further confirms that smaller particles exhibit stronger aggregation, likely due to surface charge interactions and reduced electrostatic repulsion in DI water, which may influence their adsorption behaviour with metal ions. The fractograms and radius of gyration (R_g) distributions (Fig. 4A, B and Table 1) demonstrate that the COOH-PSNPs maintained

Table 2 Pseudo-first order (PFO) and pseudo-second order (PSO) kinetic parameters for the adsorption of Cr, As, and Se onto COOH-PSNPs of different sizes (100 nm, 500 nm, 1000 nm, and mixed sizes)

	Pseudo-first-order kinetics			Pseudo-second-order kinetics		
	q_e (mg g^{-1})	K_1 (min^{-1})	R^2	q_e (mg g^{-1})	K_2 (g mg^{-1} min^{-1})	R^2
Mixed elements with 100, 500, and 1000 nm						
Cr	0.82	8.2272×10^{-4}	0.85	5.76	0.0094	0.99
As	0.45	3.53673×10^{-5}	0.10	0.99	0.0069	0.93
Se	0.20	1.09592×10^{-4}	0.05	1.24	0.0118	0.98
Mixed elements with 100 nm						
Cr	0.01	4.0133×10^{-4}	0.13	0.62	0.22	0.99
As	0.10	6.18926×10^{-4}	0.55	0.32	0.037	0.98
Se	0.06	6.74654×10^{-4}	0.72	0.23	−0.19	0.99
Mixed elements with 500 nm						
Cr	0.02	4.69531×10^{-4}	0.46	0.62	0.15	1
As	0.15	5.72366×10^{-4}	0.49	0.25	0.08	0.99
Se	0.15	4.84598×10^{-4}	0.67	0.19	0.16	0.98
Mixed elements with 1000 nm						
Cr	0.03	5.94644×10^{-4}	0.62	0.62	0.14	1
As	0.17	5.21051×10^{-4}	0.64	0.28	0.01	0.99
Se	0.17	6.11379×10^{-4}	0.79	0.22	0.012	0.99

q_e is the adsorption capacity at equilibrium, k_1 (min^{-1}) and k_2 (g mmol^{-1} min^{-1}) represent the parameters for kinetic rate constants for the pseudo-first-order and pseudo-second-order models, respectively, and R^2 is the correlation coefficient.

structural integrity after incubation with the PTEs. No significant agglomeration was observed for individual or mixed particle sizes. However, slight shoulders in the peaks of the 100 nm and 500 nm fractions indicated minor surface restructuring, likely due to metal adsorption. The R_g values in the main peaks were constant but increased slightly post-incubation with metals in the peak shoulders to 44.5 nm ± 2.3 nm for 100 nm COOH-PSNPs, to around 211.0 nm ± 3.8 nm for 500 nm COOH-PSNPs and to 429.0 nm ± 5.0 nm for 1000 nm COOH-PSNPs, supporting the conclusion that PTE binding occurred without compromising particle stability or agglomeration tendency. The angular-dependent scattering signal from the MALS detector was used to calculate particle number concentrations, which were then employed to estimate total particle surface areas. This analysis confirmed that the stability of COOH-PSNPs allowed for accurate assessment of the metal adsorption behaviour. AF4 fractionation and subsequent elemental analysis by ICP-MS revealed the presence of Cr and As absorbed onto all particle sizes (Fig. 5A–C). Se was detectable for individual size fractions but remained close to the detection limit, whereas it was not measurable on the particles in the mixed samples. The overlaid fractograms of PTE concentrations with MALS scattering signals (Fig. 6) confirmed that the adsorption trends of Cr and As were consistent across particle sizes, indicating a lack of size dependence in mixed systems.

The quantitative analysis of PTE adsorption (Table 3) on COOH-PSNPs using AF4-MALS-ICP-MS revealed significant differences based on particle size (100 nm, 500 nm, and 1000 nm) and the type of PTEs. Cr exhibited the highest adsorption across all metrics, while As demonstrated considerably lower adsorption, and Se adsorption was negligible. For Cr, the adsorption per total particle surface area increased with particle size, ranging from 9.45×10^{-15} μg nm^{-2} for 100 nm particles to 2.98×10^{-14} μg nm^{-2} for 500 nm and 6.87×10^{-14} μg nm^{-2} for 1000 nm particles. Similarly, per particle, Cr adsorption increased significantly with particle size, from 7.05×10^{-12} μg nm^{-2} for 100 nm to 5.35×10^{-10} μg nm^{-2} for 500 nm and 5.26×10^{-9} μg nm^{-2} for 1000 nm particles. When normalised to the number of COOH groups, the trend indicated that Cr adsorption was highest for 1000 nm particles (1.503×10^{-15} μg per COOH group), followed by 500 nm particles (1.407×10^{-15} μg per COOH group) and 100 nm particles (8.597×10^{-16} μg per COOH group). These results suggest that the lower density of COOH groups on larger particles reduces steric hindrance, enabling stronger interactions and greater metal ion adsorption efficiency. However, when normalised to particle mass, Cr adsorption decreased with increasing particle size, from 0.763 mg g^{-1} for 100 nm particles to 0.404 mg g^{-1} for 500 nm and 0.201 mg g^{-1} for 1000 nm particles. This indicates that smaller particles have a higher adsorption efficiency per unit mass due to their larger surface area-to-volume ratio.

In contrast, As adsorption was markedly lower. Per total particle surface area, adsorption increased with particle size, from 7.22×10^{-16} μg nm^{-2} for 100 nm particles to 2.54×10^{-15} μg nm^{-2} for 500 nm and 7.10×10^{-15} μg nm^{-2} for 1000 nm particles. Per particle, As adsorption ranged from 5.39×10^{-13} μg per particle for 100 nm particles to 4.56×10^{-11} μg per particle for 500 nm and 5.44×10^{-10} μg per particle for 1000 nm particles. When normalised to COOH groups, As adsorption was significantly lower than Cr, with values of 6.57×10^{-17} μg per COOH group for 100 nm particles, 1.207×10^{-16} μg per

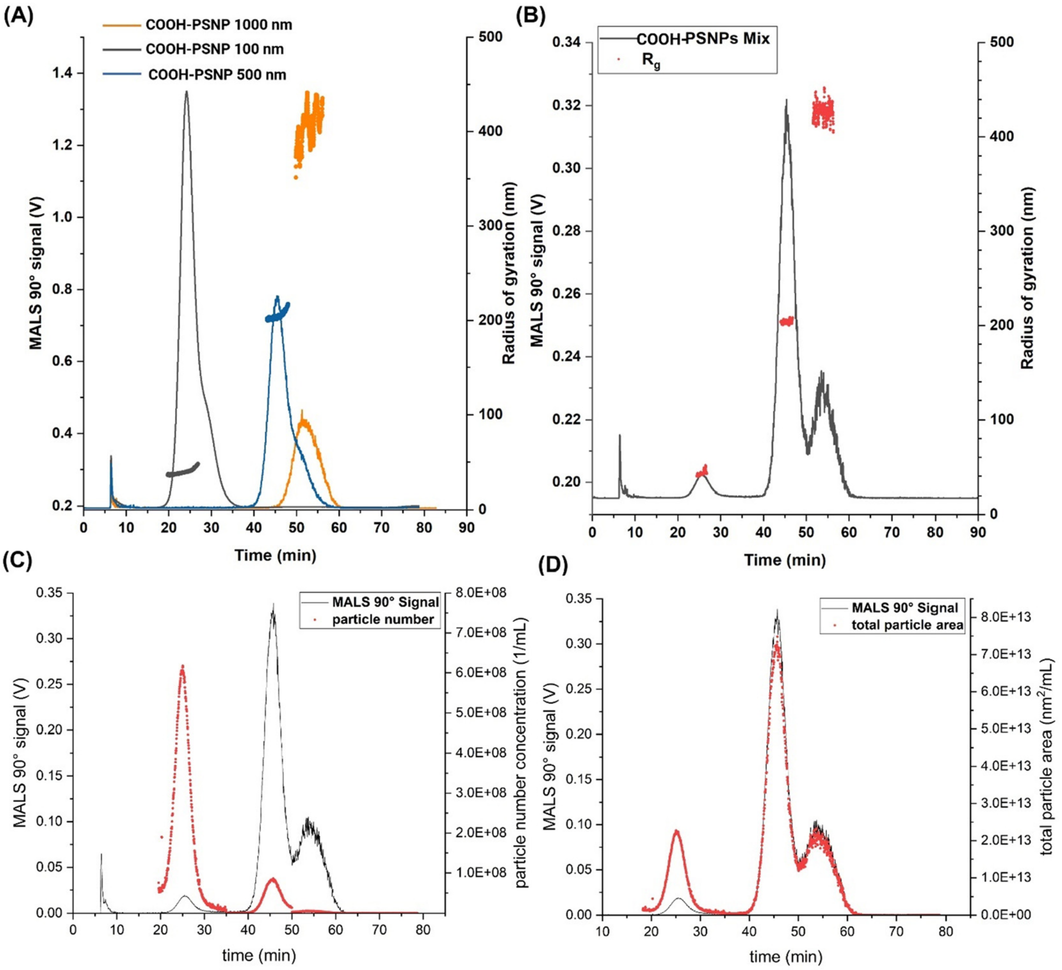

Fig. 5 Analysis of COOH-PSNP fractionation using AF4-MALS. (A) Fractograms showing the MALS 90° signal for individual COOH-PSNP sizes (100 nm, 500 nm, and 1000 nm) when dispersed in HEPES buffer, demonstrating distinct elution profiles corresponding to each particle size. The radius of gyration (R_g) for each size fraction is plotted alongside, indicating stable particle sizes with minor deviations. (B) Fractogram of the mixed COOH-PSNP sample with the MALS 90° signal and R_g. Shoulders on the peaks indicate slight structural changes after incubation with metal ions, but no significant agglomeration is observed. (C) MALS 90° signal and calculated particle number concentrations for the mixed COOH-PSNP sample. The particle number concentration closely follows the MALS signal, confirming consistent particle size distributions across fractions. (D) MALS 90° signal and total particle area for the mixed COOH-PSNP sample. The close correlation between signals suggests a stable particle morphology and size distribution post-incubation.

COOH group for 500 nm, and 1.554×10^{-17} µg per COOH group for 1000 nm. Normalisation by particle mass also reflected this trend, with As adsorption decreasing from 0.0583 mg g^{-1} for 100 nm particles to 0.0344 mg g^{-1} for 500 nm and 0.0208 mg g^{-1} for 1000 nm. These results suggest that weaker binding mechanisms, such as physisorption or outer-sphere complexation, dominate As adsorption on COOH-PSNPs. Se adsorption was negligible across all particle sizes, with values close to the detection limit of 0.18 ppb, indicating an inherently low affinity for the carboxylated surfaces of COOH-PSNPs under the experimental conditions.

The adsorption behaviour of PTEs on COOH-PSNPs is strongly influenced by particle size, surface chemistry, and the type of metal ion. Cr demonstrated high adsorption efficiency, driven by its strong chemical affinity for COOH groups, with larger particles offering enhanced adsorption due to reduced steric hindrance. As, on the other hand, exhibited weaker adsorption, likely due to its reliance on less stable physisorption mechanisms. Se's negligible adsorption highlights the importance of electrostatic compatibility and chemical affinity in determining adsorption efficiency. These findings highlight the role of surface functional group and particle size of MnPs in modulating the adsorption of specific PTEs. For Cr ions, larger particles are advantageous for bulk adsorption, while smaller particles may be more efficient for applications requiring high adsorption per unit mass.

The adsorption behaviour of Cr and As aligned closely with their intrinsic chemical affinities for the carboxyl groups on the COOH-PSNP surface. Cr consistently exhibited stronger chemisorptive interactions, reflected in its higher adsorption per particle and per unit surface area, while As showed weaker bonding, likely due to differences in binding mechanisms.

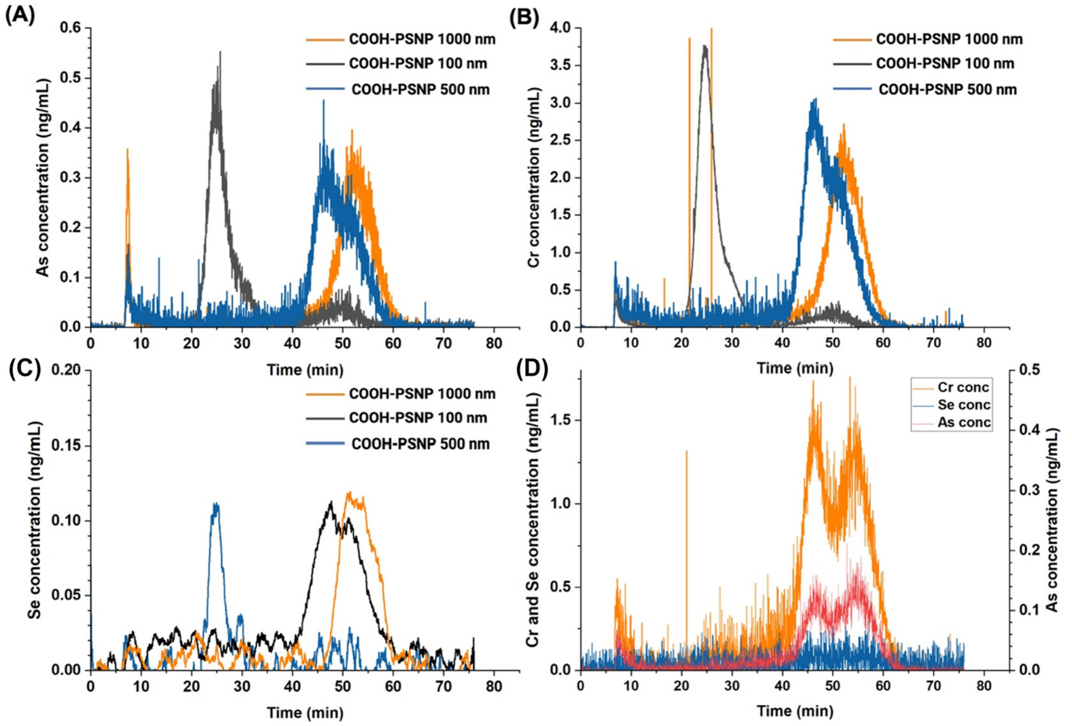

Fig. 6 Elemental analysis of PTE adsorption onto COOH-PSNPs by AF4-ICP-MS. (A) Fractograms of arsenic (As) concentration across individual COOH-PSNP sizes (100 nm, 500 nm, and 1000 nm) in the presence of As at a 1 μg mL^{-1} concentration. Distinct elution profiles indicate size-dependent As adsorption, with the highest adsorption observed for 1000 nm COOH-PSNPs. (B) Fractograms of chromium (Cr) concentration for individual COOH-PSNP sizes in the presence of Cr at a 1 μg mL^{-1} concentration, showing significantly higher Cr adsorption compared to other metals (note the *y*-axis range). The adsorption is consistent across size fractions, with distinct elution peaks for each particle size. (C) Fractograms of selenium (Se) concentration for individual COOH-PSNP sizes in the presence of Se at a 1 μg mL^{-1} concentration, revealing low adsorption levels close to the detection limit. The elution profiles are less defined compared to Cr and As, indicating weaker interactions between Se and COOH-PSNPs. (D) Combined fractograms comparing Cr, As, and Se concentrations across the size mixture (100 nm, 500 nm, and 1000 nm) of COOH-PSNPs, highlighting the dominant adsorption of Cr, followed by As, with Se exhibiting minimal adsorption.

The negligible adsorption of Se further emphasises the selectivity of COOH-PSNPs for Cr and, to a lesser extent, As. Overall, AF4-MALS-ICP-MS provided a comprehensive assessment of COOH-PSNP size-dependent adsorption behaviour. The AF4-MALS-ICP-MS fractograms (Fig. 5 and 6) and quantitative data (Table 3) collectively highlight the robustness of the methodology in elucidating the adsorption dynamics of PTEs onto MnPs. The fractograms in Fig. 6 were obtained under the same experimental conditions as those in Fig. 5, ensuring a consistent comparison of Cr, As, and Se adsorption across different particle sizes. These findings also highlight the environmental implications of Cr and As fouling on COOH-PSNPs and their potential role as vectors for PTE transport in aquatic ecosystems.

The integration of AF4-MALS and ICP-MS highlights their distinct yet complementary strengths in analysing the interactions of MnPs with metal(loid) ions. AF4-MALS-ICP-MS offers detailed insights into particle size-dependent adsorption trends and surface interactions, while ICP-MS alone quantifies the bulk metal(loid) concentrations in the solution. The analysis revealed contrasting observations. AF4-MALS-ICP-MS showed a clear decreasing trend in adsorption capacity with increasing particle size of COOH-PSNPs for all metal ions. Specifically, adsorption capacity reduced from 0.763 mg g^{-1} for 100 nm COOH-PSNPs to 0.201 mg g^{-1} for 1000 nm COOH-PSNPs (Table 3). However, ICP-MS measurements showed no significant variation in adsorption capacity with particle size, as demonstrated by the nearly constant Cr adsorption of approximately 0.62 mg g^{-1} across all sizes (Table 2). This discrepancy suggests that while ICP-MS provides a reliable bulk measurement, it may lack the resolution needed to capture the surface-level and particle-specific variations that AF4-MALS-ICP-MS can identify. Therefore, the integration of these methods underscores the complexity of adsorption processes, highlighting the influence of both particle size and analytical technique on the observed adsorption behaviour. These findings emphasise the importance of employing advanced, complementary techniques to achieve a more nuanced understanding of MnP behaviour in environmental systems. Such insights are critical for developing targeted strategies to mitigate MnP-associated pollution, particularly by addressing size-dependent interactions and their implications for pollutant transport and removal efficiency.

Table 3 Adsorption of Cr and As onto COOH-PSNPs per unit particle surface area (mass per nm^2) and per particle as determined using AF4-MALS-ICP-MS

PTE adsorption (μg per total particle surface area)					
Cr (μg)per nm^2 (PS)			As (μg) nm^{-2} (PS)		
COOH-PS100	COOH-PS500	COOH-PS1000	COOH-PS100	COOH-PS500	COOH-PS1000
9.45×10^{-15}	2.98×10^{-14}	6.87×10^{-14}	7.22×10^{-16}	2.54×10^{-15}	7.10×10^{-15}
PTE adsorption (μg per particle)					
Cr (μg) per particle			As (μg) per particle		
COOH-PS100	COOH-PS500	COOH-PS1000	COOH-PS100	COOH-PS500	COOH-PS1000
7.05×10^{-12}	5.35×10^{-10}	5.26×10^{-09}	5.39×10^{-13}	4.56×10^{-11}	5.44×10^{-10}
PTE adsorption (mg g^{-1}) of particles					
Cr (mg) per g of particle			As (mg) per g of particle		
COOH-PS100	COOH-PS500	COOH-PS1000	COOH-PS100	COOH-PS500	COOH-PS1000
0.76	0.40	0.20	0.05	0.03	0.02
PTE adsorption (μg per COOH group)					
Cr (μg) per COOH group			As (μg) per COOH group		
COOH-PS100	COOH-PS500	COOH-PS1000	COOH-PS100	COOH-PS500	COOH-PS1000
8.597×10^{-16}	1.407×10^{-15}	1.503×10^{-15}	0.657×10^{-16}	1.207×10^{-16}	1.554×10^{-16}

4. Implications and outlook

The findings of this study highlight the transformative role of AF4-MALS-ICP-MS in elucidating PTE fouling of MnPs. By enabling size-specific analysis and simultaneous characterisation of particle properties and metal adsorption, this hyphenated technique represents a marked advance over conventional ICP-MS and single-particle ICP-MS (spICP-MS) methods, which lack the same degree of size resolution and can be influenced by particle composition.

In particular, the lower size detection limit in AF4-MALS-ICP-MS is determined primarily by the ultrafiltration membrane cut-off and the MALS detector threshold—factors that are largely independent of particle type—whereas the minimum detectable size in spICP-MS depends strongly on material-specific ionisation efficiencies. While spICP-MS can achieve very low detection limits for materials such as gold and silver (due to their favourable ionisation characteristics), the detection thresholds for oxidic nanomaterials—including TiO_2 and SiO_2—are notably higher. This material dependence has been demonstrated in the literature.[54] We acknowledge that faster dwell times and improving instrumentation continue to push the detection limits of spICP-MS lower; nevertheless, these advancements remain more material-dependent than the fundamental limitations imposed by AF4-MALS. Consequently, AF4-MALS-ICP-MS provides a robust and composition-independent platform for comprehensive characterisation of MnPs and their interactions with PTEs, without compromising particle integrity.

The results reveal that Cr exhibits the highest adsorption to COOH-PSNPs among the tested metals, driven by strong chemisorptive interactions with carboxyl groups, while As and Se exhibit weaker adsorption mechanisms. Importantly, the adsorption trends were largely independent of particle size in mixed COOH-PSNP-sized systems, suggesting that intrinsic chemical affinity plays a dominant role. These insights have far-reaching implications for assessing the environmental behaviour of MnPs, particularly their role as vectors for PTEs in aquatic ecosystems.

By providing detailed and accurate quantification of PTE adsorption across size fractions, AF4-MALS-ICP-MS establishes itself as a critical method for environmental risk assessment. In contrast to spICP-MS, which is a very sensitive and fast screening technique, AF4-MALS-ICP-MS has a lower size detection limit for various MnPs and is able to efficiently characterise particle size in the presence of interfering matrices (*e.g.*, metal ions) as well as in complex media. Future studies can leverage this technique to investigate the interaction of MnPs with other environmental pollutants in complex media and particle systems and to inform the development of mitigation strategies for plastic pollution. The relevance of this work extends beyond academic research, impacting policies aimed at reducing the risks associated with MnP contamination. By bridging the gap between fundamental science and environmental monitoring, this study paves the way for advanced monitoring and regulatory frameworks to address emerging contaminants in global water systems. The AF4-MALS-ICP-MS technique is a stepping stone towards setting a new benchmark for analysing complex pollutant interactions, offering a robust approach for safeguarding ecosystems and public health.

Author contributions

S. C.: conceptualisation, experimentation, original draft, visualisation, funding acquisition, and writing – review & editing; R. D.: supervision, original draft, visualisation, and writing – review & editing; P. B.: original draft, visualisation, and writing – review & editing; N. L.: experimentation and visualisation, P. D.: visualisation and writing – review & editing; F. M.: supervision, visualisation, and writing – review & editing; I. L.: writing – review & editing, funding acquisition, and supervision.

Data availability

Data will be made available by the authors upon request.

Conflicts of interest

There are no conflicts to declare.

Acknowledgements

SC acknowledges the UKRI NERC Independent Research Fellowship (grant number UKRI187), Engineering and Physical Sciences Research Council Co-Fund ECR Impact Acceleration Account [grant number EP/X525662/1], Royal Society of Chemistry Researcher Development and Travel Grant (D24-6298205770), and DAAD, The German Academic Exchange Service short-term research grant for supporting this research. IL acknowledges the EU Horizon 2020 project CompSafeNano (Grant Agreement No. 101008099) for supporting the secondment of SC to Postnova Analytics in Germany, and the Royal Society International Exchanges grant (ES\R2\232158). IL also acknowledges the Horizon Europe grant CHIASMA (Grant Agreement No. 101137613) and the UKRI Innovate UK support for UoB participation *via* the Horizon Guarantee Fund (Grant No. 10101594). PB gratefully acknowledges the Indian Institute of Technology Gandhinagar, India, for granting the Overseas Research Experience Fellowship (OREF), which facilitated the research visit to the University of Birmingham, United Kingdom.

References

1 R. Permana, S. Chakraborty and E. Valsami-Jones, Nanoplastics in Aquatic Environments: The Hidden Impact of Aging on Fate and Toxicity, *Environ. Chem. Ecotoxicol.*, 2025, 7, 429–444, DOI: **10.1016/J.ENCECO.2025.02.007**.

2 E. Marcharla, S. Vinayagam, L. Gnanasekaran, M. Soto-Moscoso, W. H. Chen, S. Thanigaivel and S. Ganesan, Microplastics in Marine Ecosystems: A Comprehensive Review of Biological and Ecological Implications and Its Mitigation Approach Using Nanotechnology for the Sustainable Environment, *Environ. Res.*, 2024, **256**, 119181, DOI: **10.1016/J.ENVRES.2024.119181**.

3 *Measures to restrict microplastics*. **https://ec.europa.eu/commission/presscorner/detail/en/ip_23_4581** (accessed 2024-12-25).

4 G. Caruso, Microplastics as Vectors of Contaminants, *Mar. Pollut. Bull.*, 2019, **146**, 921–924, DOI: **10.1016/J.MARPOLBUL.2019.07.052**.

5 K. Prabhu, P. E. Charles, K. Jabeen, R. Rajaram, S. Paramasivam and S. Selvam, Adsorption of Heavy Metals on Microplastics in Marine Environments, in: *Meso and Microplastic Risk Assessment in Marine Environments: New Threats and Challenges*, 2024, pp. 275–292. DOI: **10.1016/B978-0-323-90980-8.00016-9**.

6 N. Khalid, M. Aqeel, A. Noman, S. M. Khan and N. Akhter, Interactions and Effects of Microplastics with Heavy Metals in Aquatic and Terrestrial Environments, *Environ. Pollut.*, 2021, **290**, 118104, DOI: **10.1016/J.ENVPOL.2021.118104**.

7 X. Shi, Z. Chen, W. Wei, J. Chen and B. J. Ni, Toxicity of Micro/Nanoplastics in the Environment: Roles of Plastisphere and Eco-Corona, *Soil Environ. Health*, 2023, **1**(1), 100002, DOI: **10.1016/J.SEH.2023.100002**.

8 N. Naqash, S. Prakash, D. Kapoor and R. Singh, Interaction of Freshwater Microplastics with Biota and Heavy Metals: A Review, *Environ. Chem. Lett.*, 2020, **18**(6), 1813–1824, DOI: **10.1007/S10311-020-01044-3**.

9 S. M. El-Sabbagh, H. I. Mira, O. A. Desouky, S. S. Hussien, D. M. Elgohary, A. O. Ali and A. M. A. El Naggar, Synthesis of Fungal Chitosan–Polystyrene Modified by Nanoparticles of Binary Metals for the Removal of Heavy Metals from Waste Aqueous Media, *RSC Adv.*, 2023, **13**(42), 29735–29748, DOI: **10.1039/D3RA04451C**.

10 A. Siripinyanond, R. M. Barnes and D. Amarasiriwardena, Flow Field-Flow Fractionation-Inductively Coupled Plasma Mass Spectrometry for Sediment Bound Trace Metal Characterization, *J. Anal. At. Spectrom.*, 2002, **17**(9), 1055–1064, DOI: **10.1039/B202734H**.

11 Q. Bai, Y. Yin, Y. Liu, H. Jiang, M. Wu, W. Wang, Z. Tan, J. Liu, M. H. Moon and B. Xing, Flow Field-Flow Fractionation Hyphenated with Inductively Coupled Plasma Mass Spectrometry: A Robust Technique for Characterization of Engineered Elemental Metal Nanoparticles in the Environment, *Appl. Spectrosc. Rev.*, 2023, **58**(2), 110–131, DOI: **10.1080/05704928.2021.1935272**.

12 B. Battistini, F. Petrucci and B. Bocca, In-House Validation of AF4-MALS-UV for Polystyrene Nanoplastic Analysis, *Anal. Bioanal. Chem.*, 2021, **413**(11), 3027–3039, DOI: **10.1007/S00216-021-03238-2/TABLES/4**.

13 D. Ruhland, K. Nwoko, M. Perez, J. Feldmann and E. M. Krupp, AF4-UV-MALS-ICP-MS/MS, SpICP-MS, and

STEM-EDX for the Characterization of Metal-Containing Nanoparticles in Gas Condensates from Petroleum Hydrocarbon Samples, *Anal. Chem.*, 2019, **91**(1), 1164–1170, DOI: 10.1021/ACS.ANALCHEM.8B05010/ASSET/IMAGES/LARGE/AC-2018-05010U_0006.JPEG.

14 B. Stolpe, L. Guo and A. M. Shiller, Binding and Transport of Rare Earth Elements by Organic and Iron-Rich Nanocolloids in Alaskan Rivers, as Revealed by Field-Flow Fractionation and ICP-MS, *Geochim. Cosmochim. Acta*, 2013, **106**, 446–462, DOI: 10.1016/J.GCA.2012.12.033.

15 L. Gfeller, A. Weber, I. Worms, V. I. Slaveykova and A. Mestrot, Mercury Mobility, Colloid Formation and Methylation in a Polluted Fluvisol as Affected by Manure Application and Flooding-Draining Cycle, *Biogeosciences*, 2021, **18**(11), 3445–3465, DOI: 10.5194/BG-18-3445-2021.

16 M. Bouby, H. Geckeis and F. W. Geyer, Application of Asymmetric Flow Field-Flow Fractionation (AsFlFFF) Coupled to Inductively Coupled Plasma Mass Spectrometry (ICPMS) to the Quantitative Characterization of Natural Colloids and Synthetic Nanoparticles, *Anal. Bioanal. Chem.*, 2008, **392**(7–8), 1447–1457, DOI: 10.1007/S00216-008-2422-0.

17 Y. Tadayon, L. Dutruch, D. Vantelon, J. Gigault, A. Dia, M. Pattier and M. Davranche, Are Nano-Colloids Controlling Rare Earth Elements Mobility or Is It the Opposite? Insight from A4F-UV-QQQ-ICP-MS, *Chemosphere*, 2024, **364**, 143164, DOI: 10.1016/J.CHEMOSPHERE.2024.143164.

18 S. Faucher, G. Charron, E. Lützen, P. Le Coustumer, D. Schaumlöffel, Y. Sivry and G. Lespes, Characterization of Polymer-Coated CdSe/ZnS Quantum Dots and Investigation of Their Behaviour in Soil Solution at Relevant Concentration by Asymmetric Flow Field-Flow Fractionation – Multi Angle Light Scattering – Inductively Coupled Plasma - Mass Spectrometry, *Anal. Chim. Acta*, 2018, **1028**, 104–112, DOI: 10.1016/J.ACA.2018.03.051.

19 I. A. M. Worms, J. Boltzman, M. Garcia and V. I. Slaveykova, Cell-Wall-Dependent Effect of Carboxyl-CdSe/ZnS Quantum Dots on Lead and Copper Availability to Green Microalgae, *Environ. Pollut.*, 2012, **167**, 27–33, DOI: 10.1016/J.ENVPOL.2012.03.030.

20 G. Xu, X. Lin and Y. Yu, Different Effects and Mechanisms of Polystyrene Micro- and Nano-Plastics on the Uptake of Heavy Metals (Cu, Zn, Pb and Cd) by Lettuce (Lactuca Sativa L.), *Environ. Pollut.*, 2023, **316**, 120656, DOI: 10.1016/J.ENVPOL.2022.120656.

21 S. Maity, C. Biswas, S. Banerjee, R. Guchhait, M. Adhikari, A. Chatterjee and K. Pramanick, Interaction of Plastic Particles with Heavy Metals and the Resulting Toxicological Impacts: A Review, *Environ. Sci. Pollut. Res. Int.*, 2021, **28**(43), 60291–60307, DOI: 10.1007/S11356-021-16448-Z.

22 Atsdr, *TOXICOLOGICAL PROFILE FOR CHROMIUM*, 2012.

23 Chromium in Drinking-Water Background Document for Development Of. 2020.

24 A. Kabata-Pendias and A. B. Mukherjee, Trace Elements from Soil to Human, in: *Trace Elements from Soil to Human*, 2007, pp. 1–550. DOI: 10.1007/978-3-540-32714-1.

25 Arsenic Compound Hazard Summary.

26 P. L. Smedley and D. G. Kinniburgh, A Review of the Source, Behaviour and Distribution of Arsenic in Natural Waters, *Appl. Geochem.*, 2002, **17**(5), 517–568, DOI: 10.1016/S0883-2927(02)00018-5.

27 G. D. Gebreeyessus and F. Zewge, A Review on Environmental Selenium Issues, *SN Appl. Sci.*, 2019, **1**(1), 1–19, DOI: 10.1007/S42452-018-0032-9/FIGURES/13.

28 F. Fordyce, Selenium Geochemistry and Health, *AMBIO: A Journal of the Human Environment*, 2007, **36**(1), 94–97, DOI: 10.1579/0044-7447(2007)36.

29 M. Kerker, *{CHAPTER} 3 - Scattering by a Sphere*, 1969, vol. 16.

30 C. R. de Bruin, E. de Rijke, A. P. van Wezel and A. Astefanei, Methodologies to Characterize, Identify and Quantify Nano- and Sub-Micron Sized Plastics in Relevant Media for Human Exposure: A Critical Review, *Environ. Sci.: Adv.*, 2022, **1**(3), 238–258, DOI: 10.1039/D1VA00024A.

31 S. Yu, M. Shen, S. Li, Y. Fu, D. Zhang, H. Liu and J. Liu, Aggregation Kinetics of Different Surface-Modified Polystyrene Nanoparticles in Monovalent and Divalent Electrolytes, *Environ. Pollut.*, 2019, **255**, 113302, DOI: 10.1016/J.ENVPOL.2019.113302.

32 G. Baier, C. Costa, A. Zeller, D. Baumann, C. Sayer, P. H. H. Araujo, V. Mailänder, A. Musyanovych and K. Landfester, BSA Adsorption on Differently Charged Polystyrene Nanoparticles Using Isothermal Titration Calorimetry and the Influence on Cellular Uptake, *Macromol. Biosci.*, 2011, **11**(5), 628–638, DOI: 10.1002/MABI.201000395.

33 Z. Wang, T. Lin and W. Chen, Occurrence and Removal of Microplastics in an Advanced Drinking Water Treatment Plant (ADWTP), *Sci. Total Environ.*, 2020, **700**, 134520, DOI: 10.1016/J.SCITOTENV.2019.134520.

34 M. Siek, K. Kandere-Grzybowska and B. A. Grzybowski, Mixed-Charge, PH-Responsive Nanoparticles for Selective Interactions with Cells, Organelles, and Bacteria, *Acc. Mater. Res.*, 2020, **1**(3), 188–200, DOI: 10.1021/ACCOUNTSMR.0C00041/ASSET/IMAGES/LARGE/MR0C00041_0008.JPEG.

35 X. Mamtimin, W. Song, Y. Wang and N. Habibul, Arsenic Adsorption by Carboxylate and Amino Modified Polystyrene Micro- and Nanoplastics: Kinetics and Mechanisms, *Environ. Sci. Pollut. Res. Int.*, 2023, **30**(15), 44878–44892, DOI: 10.1007/S11356-023-25475-X.

36 M. Sultana, M. H. Rownok, M. Sabrin, M. H. Rahaman and S. M. N. Alam, A Review on Experimental Chemically Modified Activated Carbon to Enhance Dye and Heavy Metals Adsorption, *Clean. Eng. Technol.*, 2022, **6**, 100382, DOI: 10.1016/J.CLET.2021.100382.

37 N. Xie, H. Wang and C. You, Role of Oxygen Functional Groups in Pb2+ Adsorption from Aqueous Solution on Carbonaceous Surface: A Density Functional Theory Study, *J. Hazard. Mater.*, 2021, **405**, 124221, DOI: 10.1016/J.JHAZMAT.2020.124221.

38 M. V. Blber and W. Stumm, An In-Situ ATR-FTIR Study: The Surface Coordination of Salicylic Acid on Aluminum and

Iron(III) Oxides, *Environ. Solution Technol.*, 1994, **28**, 763–768.

39 K. A. Moltved and K. P. Kepp, The Chemical Bond between Transition Metals and Oxygen: Electronegativity, d-Orbital Effects, and Oxophilicity as Descriptors of Metal–Oxygen Interactions, *J. Phys. Chem. C*, 2019, **123**, 39, DOI: 10.1021/acs.jpcc.9b04317.

40 Y. Dong, M. Gao, Z. Song and W. Qiu, As(III) Adsorption onto Different-Sized Polystyrene Microplastic Particles and Its Mechanism, *Chemosphere*, 2020, **239**, 124792, DOI: 10.1016/J.CHEMOSPHERE.2019.124792.

41 N. Narwal, M. Adnan Kakakhel, D. Katyal, S. Yadav, P. K. Rose, E. R. Rene, M. R. J. Rakib, K. S. Khoo and N. Kataria, Interactions Between Microplastic and Heavy Metals in the Aquatic Environment: Implications for Toxicity and Mitigation Strategies, *Water, Air, Soil Pollut.*, 2024, **235**(9), 1–26, DOI: 10.1007/S11270-024-07343-7.

42 G. Liu, P. H. Dave, R. W. M. Kwong, M. Wu and H. Zhong, Influence of Microplastics on the Mobility, Bioavailability, and Toxicity of Heavy Metals: A Review, *Bull. Environ. Contam. Toxicol.*, 2021, **107**(4), 710–721, DOI: 10.1007/S00128-021-03339-9/TABLES/2.

43 B. Liu, Y.-N. Xin, J. Zou, F. M. Khoso, Y.-P. Liu, X.-Y. Jiang, S. Peng, J.-G. Yu, B. Liu, Y.-N. Xin, J. Zou, F. M. Khoso, Y.-P. Liu, X.-Y. Jiang, S. Peng and J.-G. Yu, Removal of Chromium Species by Adsorption: Fundamental Principles, Newly Developed Adsorbents and Future Perspectives, *Molecules*, 2023, **28**(2), 639, DOI: 10.3390/MOLECULES28020639.

44 Z. Fang, Z. Wang, H. Tang and A. Hursthouse, Comparison of Hexavalent Chromium Adsorption Behavior on Conventional and Biodegradable Microplastics, *Water*, 2024, **16**(14), 2050, DOI: 10.3390/W16142050.

45 I. Zwolak, The Role of Selenium in Arsenic and Cadmium Toxicity: An Updated Review of Scientific Literature, *Biol. Trace Elem. Res.*, 2019, **193**(1), 44–63, DOI: 10.1007/S12011-019-01691-W.

46 S. Goldberg, C. T. Johnston and G. E. Brown, Mechanisms of Arsenic Adsorption on Amorphous Oxides Evaluated Using Macroscopic Measurements, Vibrational Spectroscopy, and Surface Complexation Modeling, *J. Colloid Interface Sci.*, 2001, **234**, 204–216, DOI: 10.1006/jcis.2000.7295.

47 H. E. Abdelwahab, M. Elhag and M. M. El Sadek, Removal of As(V) and Cr(VI) Using Quinoxaline Chitosan Schiff Base: Synthesis, Characterization and Adsorption Mechanism, *BMC Chem.*, 2024, **18**(1), 1–19, DOI: 10.1186/S13065-024-01328-7/FIGURES/9.

48 K. S. Patel, P. K. Pandey, P. Martín-Ramos, W. T. Corns, S. Varol, P. Bhattacharya and Y. Zhu, A Review on Arsenic in the Environment: Contamination, Mobility, Sources, and Exposure, *RSC Adv.*, 2023, **13**(13), 8803–8821, DOI: 10.1039/D3RA00789H.

49 Y. Peng, Y. Shen, M. Ge, Z. Pan, W. Chen and B. Gong, Efficient Extraction of Heavy Metals from Collagens by Sulfonated Polystyrene Nanospheres, *Food Chem.*, 2019, **275**, 377–384, DOI: 10.1016/J.FOODCHEM.2018.09.111.

50 R. Wu, B. Hong, C. Xue, Z. Chen and Z. Chen, ZIF-8 Used for the Selective Recovery of Heavy Rare Earth Elements from Mining Wastewater, *Environ. Sci. Technol.*, 2024, **58**(22), 9612–9623, DOI: 10.1021/ACS.EST.3C10653/ASSET/IMAGES/LARGE/ES3C10653_0006.JPEG.

51 Z. Jia, F. Liang, X. Xu, H. Zhou, Y. Zhang and P. Liang, One-Pot Amination and Carboxylation Functionalization of Lignin for Efficient Adsorption of Cr(VI) and Cd(II): Influence of Functional Groups on Adsorption Equilibrium and Mechanism, *Colloids Surf., A*, 2024, **703**, 135278, DOI: 10.1016/J.COLSURFA.2024.135278.

52 A. Benko, J. Duch, M. Gajewska, M. Marzec, A. Bernasik, M. Nocuń, W. Piskorz and A. Kotarba, Covalently Bonded Surface Functional Groups on Carbon Nanotubes: From Molecular Modeling to Practical Applications, *Nanoscale*, 2021, **13**(22), 10152–10166, DOI: 10.1039/D0NR09057C.

53 F. Abdel-Wahab, M. Abdel-Baki, S. Ibrahim, M. Abdelnabi and H. Abdelmaksoud, Investigation of Oxygen Defects in Chromium-Doped Borosilicate Glass Co-Doped with Alkali Metal (Na2O) and Transition Metal (ZnO) for Photonic Applications, *Appl. Phys. A:Mater. Sci. Process.*, 2025, **131**(1), 1–23, DOI: 10.1007/S00339-024-08114-1/FIGURES/15.

54 S. Lee, X. Bi, R. B. Reed, J. F. Ranville, P. Herckes and P. Westerhoff, Nanoparticle Size Detection Limits by Single Particle ICP-MS for 40 Elements, *Environ. Sci. Technol.*, 2014, **48**(17), 10291–10300, DOI: 10.1021/ES502422V/SUPPL_FILE/ES502422V_SI_001.PDF.